Draft version March 16, 2020
Preprint typeset using LaTeX style AASTeX6 v. 1.0

ASTEROIDS' SIZE DISTRIBUTION AND COLORS FROM HITS

J. Peña[1,2], C. Fuentes[1,2], F. Förster[3,2], J. Martínez-Palomera[4,1,3], G. Cabrera-Vives[5,2] J.C. Maureira[3], P. Huijse[6, 2], P.A. Estévez[7,2], L. Galbany[8], S. González-Gaitán[9, 3, 2], Th. de Jaeger[4, 1, 2]

[1]Departamento de Astronomía, Universidad de Chile, Camino del Observatorio 1515, Las Condes, Santiago, Chile.
[2]Millennium Institute of Astrophysics, Chile.
[3]Center for Mathematical Modeling, Beaucheff 851, 7th floor, Santiago, Chile.
[4]Department of Astronomy, University of California, Berkeley, CA 94720-3411, USA.
[5]Department of Computer Science, Universidad de Concepción, Chile.
[6]Informatics Institute, Universidad Austral de Chile, Chile.
[7]Electrical Engineering Department, University of Chile, Chile.
[8]Departamento de Física Teórica y del Cosmos, Universidad de Granada, E-18071 Granada, Spain.
[9]CENTRA, Instituto Superior Técnico, Universidade de Lisboa, Portugal.

ABSTRACT

We report the observations of solar system objects during the 2015 campaign of the High cadence Transient Survey (HiTS). We found 5740 bodies (mostly Main Belt asteroids), 1203 of which were detected in different nights and in g' and r'. Objects were linked in the barycenter system and their orbital parameters were computed assuming Keplerian motion. We identified 6 near Earth objects, 1738 Main Belt asteroids and 4 Trans-Neptunian objects. We did not find a $g'-r'$ color–size correlation for $14 < H_{g'} < 18$ ($1 < D < 10$ km) asteroids. We show asteroids' colors are disturbed by HiTS' 1.6 hour cadence and estimate that observations should be separated by at most 14 minutes to avoid confusion in future wide-field surveys like LSST. The size distribution for the Main Belt objects can be characterized as a simple power law with slope ~ 0.9 , steeper than in any other survey, while data from HiTS 2014's campaign is consistent with previous ones (slopes ~ 0.68 at the bright end and ~ 0.34 at the faint end). This difference is likely due to the ecliptic distribution of the Main Belt since 2015's campaign surveyed farther from the ecliptic than did 2014's and most previous surveys.

Keywords: Minor planets (1065), Photometry (1234), Sky surveys (1464), Main belt asteroids (2036)

1. INTRODUCTION

Our solar system (SS) is currently understood to have emerged from a protoplanetary disk (Armitage 2017 and references therein). While planets grew and migrated (see Horner et al. 2013 for a summary), thousands of planetesimals formed, grew bigger and broke into smaller pieces in a process that can still be studied in the stable reservoirs of minor bodies, namely the Main Belt (MB), Jovian Trojans, Neptunian Trojans, and Trans-Neptunian Objects (TNOs) (Sheppard & Trujillo 2006). This evolution has left its mark in the orbital distribution of the Main Belt and in its size distribution (SD).

The SD provides a direct glimpse into the collisional history of minor bodies. Under collisional equilibrium the SD is described by a power law $N(H) \propto 10^{\alpha H}$ and $N(D) \propto D^{-q}$ (H the absolute magnitude and D the body's diameter, with $q = 5\alpha + 1$) with $q = 3.5$ and $\alpha = 0.5$ (Dohnanyi 1969). In Table 1 we provide a summary of Main Belt surveys, including SD best fit and filter information. Having multiple filters provides asteroids' surface colors that might be related to composition and collisional history.

Ivezić et al. (2001) analyzed Sloan Digital Sky Survey (SDSS) data (York et al. 2000) and separated the MB by color, finding $\alpha \sim 0.61 \pm 0.01$ for brighter bodies while they found $\alpha = 0.24 \pm 0.01$ for *"red"* bodies, $\alpha = 0.28 \pm 0.01$ for *"blue"* bodies and 0.25 ± 0.01 for *"blue"* and *"red"* combined (*"red"* and *"blue"* by their definition, associated to S-type and C-type respectively). For S-type and C-type asteroids, they found both their SDs to have a break at $D \sim 5$ km, and attributed this feature to a color-size dependence for bodies smaller than 5 km. Parker et al. (2008), using a more updated data set (an early version of the 4th release of the SDSS Moving Object Catalog, Ivezić et al.

jpena@das.uchile.cl

2010) divided the MB by semi-major axis a and analyzed the absolute magnitude H, finding similar slopes for bright bodies but steeper slopes for smaller objects ($\alpha \sim 0.42$). In both cases they found the SD gets flatter with a. Parker et al. (2008) also analyzed individual asteroid families, finding slopes α varying from 0.37 to 1.04 at the bright end and α from 0.1 to 0.62 at the faint end. Yoshida et al. (2003) analyzed the size distribution for ~ 1000 small asteroids from SMBAS (Subaru Main Belt Asteroid Survey). Observations were only separated by $\sim$2 hours, affording only rough distance estimates. They report no break with a single power slope $q = 2.19 \pm 0.02$ ($\alpha = 0.24$) for the entire MB SD (for $D > 0.5$ km) which is similar to the one found by Ivezić et al. (2001) in SDSS. They also found that the SD gets flatter with a.

Yoshida & Nakamura (2007) using a new set of data from SMBAS measured $B - R$ and H, getting broken power laws for small bodies: $q = 2.29 \pm 0.02$ ($\alpha = 0.26$, similar to faint bodies from Ivezić et al. 2001) for small objects ($D < 1$ km) and $q = 2.75 \pm 0.02$ ($\alpha = 0.35$) for bright objects (between the values from Ivezić et al. 2001 and Parker et al. 2008); they also separated the bodies by color (based on a slight low density in their color histograms), finding that S-like (redder) bodies have $q = 2.29 \pm 0.02$ ($\alpha = 0.26$) at the faint end ($D < 1$ km) and $q = 3.44 \pm 0.09$ ($\alpha = 0.49$) at the bright end, while C-like (bluer) bodies could be characterized by a single slope of $q = 2.33 \pm 0.03$ ($\alpha = 0.27$). Lin et al. (2015) analyzed 150 asteroids finding an SD compatible with the slopes found by Yoshida & Nakamura (2007); they also found that S-like bodies are more common in the inner region of the MB while C-like bodies dominate the region beyond 2.82 au of the MB. Wiegert et al. (2007) analyzed 1525 MB bodies with an arc of $\leqslant 2$ days measured in g' or in r' with the Canada-France-Hawaii Telescope (CFHT); they found a very clear difference of slopes between g' and r' and a varying slope with distance, getting a steeper slope between $2.6 < a < 3.0$ au (parameter obtained assuming circular orbits); these results were discarded by August & Wiegert (2013) because they used data beyond the limiting magnitude. August & Wiegert (2013) used $\sim 17,000$ MB bodies from CFHT Legacy Survey (CFHTLS) with measurements in g' and r', getting $\alpha = 0.39 \pm 0.01$ in g' and r' for all bodies without finding a color-size dependence, but they do recover a flatter slope at higher distance (all of this between $15 < H < 17$). August & Wiegert (2013) suggest this slope-distance dependence is produced by a difference in composition, in that the inner MB is dominated by S–type bodies and the outer MB by C–type, although they do mention that it is not clear how this differentiation affects the slope and they do not do a color analysis such as that of Ivezić et al. (2001) and Yoshida & Nakamura (2007). One year earlier, Gladman et al. (2009) analyzed $\sim$ 1000 small bodies with time ranges of more than three nights (in the Subkilometer asteroid diameter survey, SKADS), allowing a good calculation of H, finding $\alpha = 0.38$ (in between the ones found by Ivezić et al. 2001 and Parker et al. 2008, but very similar to the one by August & Wiegert 2013). SKADS also has color measurements, but Gladman et al. (2009) did not find any bimodality as in SDSS (Ivezić et al. 2001) or as claimed in Yoshida & Nakamura (2007). Masiero et al. (2011) computed asteroid diameters from *Wide-field Infrared Survey Explorer* (WISE) data (Wright et al. 2010) and found that the SD follows a slope similar to the one find by Gladman et al. (2008) for small bodies. Ryan et al. (2015) analyzed $\lesssim$ 2000 from *Spitzer*'s MIPSGAL and Taurus surveys (Carey et al 2009; Rebull et al. 2010), obtaining $q = 3.34 \pm 0.05$ ($\alpha = 0.47 \pm 0.01$) for MB bodies between 2 and 25 km (which seems an in-between value from bright and faint slopes from previous surveys such as SDSS), and different slope values when separating by taxonomic type, although it seems they do not take into consideration their completeness limit (of 6.65 km or 15.75 in H according to them). In summary, there is a wide range of values for the α parameter, especially for faint bodies ($D \lesssim 5$ km). This is probably caused by differences in data reduction, orbital parameter determination and limiting magnitudes of each work. The most complete data set comes from SDSS (which uses known bodies for their orbital parameters), getting $\alpha \sim 0.61$ for bright bodies. For faint bodies, the values vary from 0.25 (Ivezić et al. 2001) to 0.38 by Gladman et al. (2009) (which is the largest survey published with good orbital parameter estimations) to ~ 0.42 by Parker et al. (2008) (again in SDSS). Many of these surveys have found that the SDs get flatter with a, while only some of these studies have found a slight color-size dependence.

In this paper we show our results finding asteroids in the 2015A campaign of the High cadence Transient Survey (HiTS). A fraction of our data ($\sim$1,700) have measured arcs of $\sim$24 hours, allowing acceptable orbital solution for H analysis. We also have $g' - r'$ for $\sim$1,200 of them, allowing some color analysis. In section 2, we present the HiTS data. In section 3 we explain our detection linking algorithm to get the different asteroids. In section 4 we show our results: orbital parameters distribution, apparent and absolute magnitude distribution and color analysis (mainly for Main Belt objects). Finally, in section 5 we present our conclusions for the 2015A campaign and we put them in contrast to results from 2014A campaign.

Table 1. Summary of SD slopes from different surveys

Survey	Date[a]	m_{lim}	Population	Criterion	N[b]	α[c]	Size Range
SDSS[d]	2001	$r* < 21.5$	MB	$1.5 \lesssim a \lesssim 4$au	670,000	$0.61 \pm .01$	$D > 5$km $(H \lesssim 15.7)$
						$0.25 \pm .01$	$D < 5$km $(H \gtrsim 15.7)$
			"blue"	$a^* < 0$	467,000	$0.61 \pm .01$	$D > 5$km
						$0.28 \pm .01$	$D < 5$km
			"red"	$a^* > 0$	203,000	$0.61 \pm .01$	$D > 5$km
						$0.24 \pm .01$	$D < 5$km
SMBS[e]	2003	$R < 24.4$	MB	$2 < a < 3.5$au	~ 500	$0.238 \pm .004$	$.5 < D < 1$km $(18.3 < H_R < 19.8)$
			inner MB	$2 < a < 2.6$au	~ 200[f]	$0.274 \pm .006$	$.23 < D < 1$km $(18.3 < H_R < 21.4)$
			middle MB	$2.6 < a < 3.0$au	~ 250[f]	$0.230 \pm .006$	$.34 < D < 1$km $(18.3 < H_R < 20.6)$
			outer MB	$3.0 < a < 3.5au$	~ 50[f]	$0.196 \pm .006$	$.49 < D < 1$km $(18.3 < H_R < 19.8)$
SMBS[g]	2007	$R < 25$	MB	$2 < a < 3.5$au	~ 800	$0.258 \pm .004$	$D < 1$km $(17.8 < H < 20.2)$
					~ 200	$0.350 \pm .004$	$D > 1$km $(14.6 < H < 17.4)$
			S–like	$B - R > 1.1$	$--$	$0.058 \pm .004$	$0.3 < D < 1$km $(17.4 < H < 20.2)$
					$--$	$0.488 \pm .018$	$D > 1$km $(15.4 < H < 17.0)$
			C–like	$B - R < 1.1$	$--$	$0.266 \pm .006$	$D > 0.6$km $(14.6 < H < 20.2)$
CFHTLS[h]	2007	$g' < 22.5$	MB	$2.0 < a < 3.5$au	185	0.37 ± 0.01	$0.6 < D < 10$km
			inner MB	$2.0 < a < 2.6$au	77	0.316 ± 0.012	$0.6 < D < 4$km
			middle MB	$2.6 < a < 3.0$au	79	0.370 ± 0.012	$0.8 < D < 6.3$km
			outer MB	$3.0 < a < 3.5$au	29	0.320 ± 0.014	$1 < D < 6.3$km
		$r' < 21.75$	MB	$2.0 < a < 3.5$au	423	0.488 ± 0.014	$1 < D < 10$km
			inner MB	$2.0 < a < 2.6$au	238	0.40 ± 0.01	$1 < D < 7.9$km
			middle MB	$2.6 < a < 3.0$au	143	0.478 ± 0.014	$1.3 < D < 7.9$km
			outer MB	$3.0 < a < 3.5$au	42	0.45 ± 0.016	$1.6 < D < 6.3$km
SDSS[i]	2008	$r' < 21.5$	inner MB	$2.0 < a < 2.5$au	30,702	0.76	$H < 14$ $(D > 7\text{km})^*$
						0.46	$H > 14$
			middle MB	$2.5 < a < 2.82$au	32,500	0.73	$H < 13.5$ $(D > 9\text{km})^*$
						0.42	$H > 13.5$
			outer MB	$2.82 < a < 3.6$au	24,367	0.56	$H < 13.5$
						0.4	$H > 13.5$
SKADS[j]	2009	$R < 23.5$	MB	$2.0 < a < 4.0$au	~ 1000	0.38	$14.8 < H_R < 17.4$ $(1 < D < 5\text{km})^{**}$
CFHTLS[k]	2013	$g' \lesssim 23$	MB	$2.0 < a < 4.0$au	7285	0.39 ± 0.01	$15 < H_{g'} < 17.6$ $(1 < D < 5\text{km})$
			inner MB	$2.0 < a < 3.0$au	–	0.39 ± 0.02	$15 < H_{g'} < 17.6$
			outer MB	$3.0 < a < 4.0$au	–	0.35 ± 0.01	$15 < H_{g'} < 17.6$
		$r' < 22.5$	MB	$2.0 < a < 4.0$au	9671	0.39 ± 0.01	$15 < H_{g'} < 17.1$
			inner MB	$2.0 < a < 3.0$au	–	0.39 ± 0.01	$15 < H_{g'} < 17.1$
			outer MB	$3.0 < a < 4.0$au	–	0.365 ± 0.004	$15 < H_{g'} < 17.1$
Spitzer's[l]	2015	–	MB	$2.06 < a < 3.65$au	1865	0.47 ± 0.01	$2 < D < 25$km
			C-Type	$p_V < 0.08$	~ 600	0.52 ± 0.01	$5 < D < 25$km
			S-Type	$0.15 < p_V < 0.35$	~ 400	0.38 ± 0.02	$5 < D < 25$km
HiTS 2014	this work	$g' < 22.5$	MB	$1.3 < a < 4.2$au	1,729	$0.68^{+0.17}_{-0.09}$	$11 < H_{g'} < 14$ $(10 \lesssim D \lesssim 30\text{km})$
						$0.34^{+0.04}_{-0.11}$	$14 < H_{g'} < 17$ $(1 \lesssim D \lesssim 10\text{km})$
HiTS 2015	this work	$g' < 22$	MB	$1.3 < a < 4.2$au	129	$0.88^{+0.09}_{-0.08}$	$14 < H_{g'} < 16.5$ $(1 \lesssim D \lesssim 10\text{km})$

Table 1 continued

Table 1 *(continued)*

Survey	Date[a]	m_{lim}	Population	Criterion	N[b]	α[c]	Size Range

[a] Publication date of the study.
[b] Number of bodies used in the analysis.
[c] Slope of the SD using H
[d] Ivezić et al. (2001)
[e] Yoshida et al. (2003)
[f] From Figure 11 in Yoshida et al. (2003)
[g] Yoshida & Nakamura (2007)
[h] Wiegert et al. (2007)
[i] Parker et al. (2008)
[j] Gladman et al. (2009)
[k] August & Wiegert (2013)
[l] Ryan et al. (2015)
[*] D calculated using albedo $p_V = 0.1$
[**] D calculated using albedo $p_V = 0.1$ and an average color of $V - R \simeq 0.4$ (see Figure 15 in Gladman et al. (2009)

2. DATA

2.1. *HiTS observations*

HiTS was a survey aimed to discover and follow up transients, especially the earliest hours of supernova explosions. For this, it combined high cadence with a high limiting magnitude and a wide field of view. These characteristics offer the opportunity to do science in various topics other than supernovae (Förster et al. 2016, 2018) such as RR Lyrae (Medina et al. 2017, 2018), SS minor bodies (Peña et al. 2018 and this work) and automatic classification of variable sources (Martínez-Palomera et al. 2018).

HiTS observations were obtained with the Dark Energy Camera (DECam) mounted at the prime focus of the Blanco 4m telescope at the Cerro-Tololo International Observatory. DECam covers a 3 square degree field of view with a mosaic of ~ 60 ccd of 2Kx4K pixels, yielding a $0.27''$/pixel resolution (DePoy et al. 2008).

HiTS was run in three different campaigns: the 2013A, 2014A and 2015A. The 2013A campaign observed 40 DECam fields (120 deg^2) every 2 hours (exposures of 173 s) during 4 nights in u' band. In 2014A we observed 40 DECam fields (120 deg^2) every 2 hours (exposures of 160 s) during 5 nights in g' band. The 2015A campaign consisted of 6 consecutive nights surveying 50 DECam fields (150 deg^2) with a cadence of 1.6 hours (exposures of 87 s) in g' band. The 2015A data are not as deep as in the 2014A campaign but survey a wider area and increase the number of visits per night from 5 to 6. These 6 nights were followed by three nonconsecutive half nights 2, 5 and 20 nights after the end of the main run. Some of the DECam pointings during the 2015A campaign were observed in r' and i' bands, but not more that once per night (and only in a few nights). The details of HiTS can be found in Förster et al. (2016), along with a comparative table of its three campaigns. In this work we used data from the 2015A campaign and results from the 2014A campaign (Peña et al. 2018). Since HiTS was not designed for asteroid observations, all asteroids observations were serendipitous. In 2014A the observations reached the ecliptic, while 2015A observations are at least 5° away from the ecliptic. The ecliptic distribution of the observations in both campaigns is shown in Figure 1.

2.2. *Data Processing*

The data used for this work were processed and reduced in the same way as done for the 2014A campaign (see Förster et al. 2016 and Cabrera-Vives et al. 2017), meaning that we had astrometry and photometry of moving objects and a probability for each of them of being real or bogus obtained using deep learning.

An incongruity in the way reduced data from a few epochs for the 2015A campaign were stored produced some uncertainty in the actual observation time for detections in those epochs. To remedy this issue, we took advantage of a new reduction (using another pipeline,

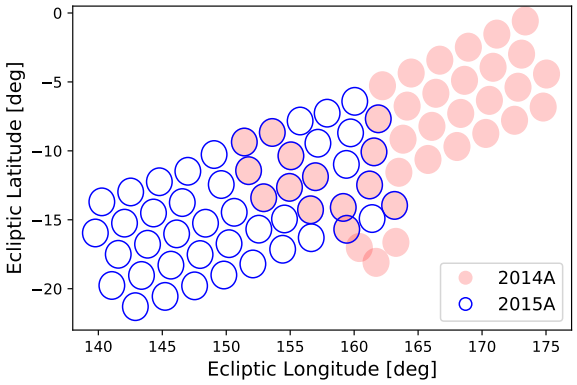

Figure 1. HiTS pointings for the 2014A and 2015A campaigns in geocentric ecliptic coordinates.

see section 3 of Martínez-Palomera et al. 2018) that had the correct observation times but without their probability of being real or bogus. We took the old data (with possible inconsistencies in their observation time) and we matched their positions with those detections of the new reduction; so if more than fifty percent of detections were within 2 pixels from the old data set to the new one for a given exposure, we considered that the data from that exposure had the correct observation time stored and we kept using those old detections, allowing us to discriminate between them to keep those with high probability of being real. After this *quality control*, we decided not to use data from 4 entire fields and 13 exposures from different fields that showed too large distances between detections from the new and old databases or have not enough detections to compare. Two of those rejected fields were among the closest to the ecliptic. Finally we ended up with 154,444 detections of moving objects with a probability of being real higher than 0.5. This is less than half of detections from the 2014A campaign. Although for 2015A we had data of 7 more fields than in 2014A, the fewer data can be explained by the limiting magnitude of 0.5 to 1 magnitudes brighter (because of the smaller exposure time and bad weather) and because in 2015A the observations were at least $\sim$ 6 degrees away from the ecliptic while 2014A data reached it.

2.3. *Survey Efficiency*

As for the 2014A data, we used the estimated position of known asteroids to test the asteroid detection efficiency of the HiTS 2015A survey. By checking the number of times a known asteroid is detected as a variable source we got an accurate assessment of the maximum number of asteroids our linking algorithm can identify as a moving object.

But first we had to decide how far a detection can be from the estimated position of a known body to consider it as *"recognized."* We had previously used information from the Minor Planet Center[1] (MPC) to look for bodies within 1.25 degrees of any DECam pointing in HiTS 2015A, but the necessity of having updated coordinates of these bodies led us to use the Jet Propulsion Laboratory (JPL) web service[2] (which gave us computational simplicity for big queries) to get the coordinates of those same asteroids. Using the coordinates of known bodies obtained this way, we computed the distance between JPL and HiTS detections, yielding the distribution shown in Figure 2. Is remarkable that using data from JPL we concentrated the difference to a much smaller range, allowing us to easily reduce our criteria for recognizing detections to a 4″ distance (in comparison to the 7″ in Peña et al. 2018).

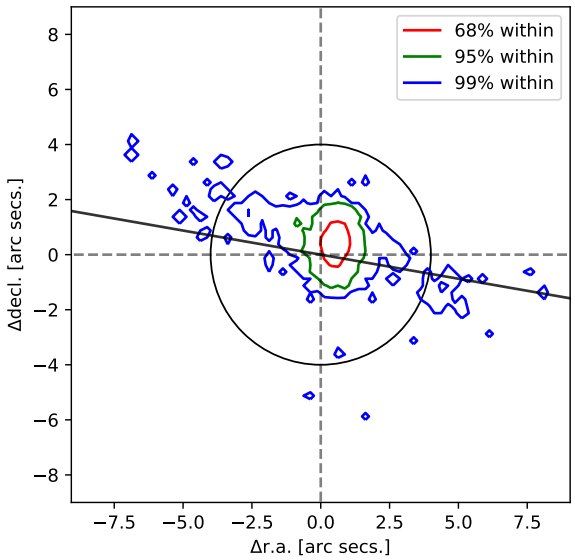

Figure 2. Contour plot for the difference between coordinates of JPL and HiTS data. Each contour surrounds a percentage of the matched data. The straight black line has the same slope as the ecliptic. The black circle has a 4″ radius.

Using the recognized detections, we could see how many of the known bodies we found. In Figure 3 we show the number of asteroids as a function of the number of detections. In gray we show those that are found only in one or two detections and in blue those found three or more times. But since our linking algorithm required at least three detections per night (Section 3), we show in orange the subset of asteroids satisfying that condition.

[1] Information provided via web page at https://www.minorplanetcenter.net/cgi-bin/checkmp.cgi

[2] JPL Horizons: https://ssd.jpl.nasa.gov/horizons.cgi

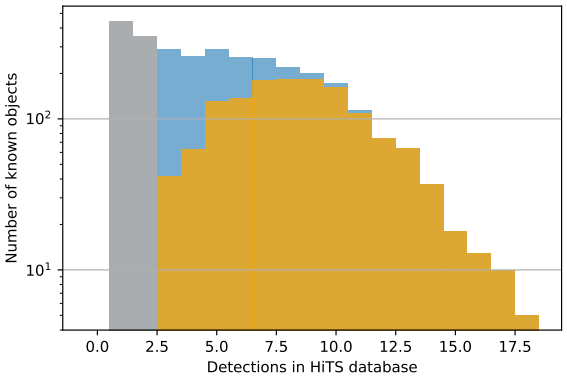

Figure 3. Histogram of number of times a known asteroid was imaged and analyzed as a variable candidate source by the HiTS survey. All known asteroids (from MPC) that were within 1.25 degrees of any DECam pointing in the HiTS survey during 2015 were considered in this analysis (using coordinates delivered by JPL). Asteroids with fewer than three detections are shown in gray, those with three or more are colored blue and those with at least three detections in a single night are shown in orange.

3. ANALYSIS

Since the detections with a probability of being real higher than 0.5 were more sparse than those in the 2014 campaign, linking detections for one night to another proved to be harder than in Peña et al. (2018). To solve this, we first found *tracklets* (sets of at least three detections that assimilate a linear trajectory in *one* night). To link different tracklets between nights we tried three different algorithms. Finally we got a collections of *tracks* (composed by 1 or more linked tracklets).

In the first algorithm we tried, we took pairs of tracklets. If their estimated position in three different times (conveniently chosen for each pair to fall in the middle of them and near each tracklet) fell near each other, then we joined these tracklets. The positions were estimated using quadratic fitting of the tracklets. How far apart the estimated positions could be depended on how far they were from the tracklets (until a maximum distance of $\sim 20''$). But finally this algorithm failed to link several known asteroids (such as the ones shown in Figure 4). Since we needed tracks to be in at least 2 nights to have good orbital parameter estimation (see section 4.1) we realized we needed a better algorithm.

The second algorithm we tried was HelioLink (Holman et al. 2018), which takes the method shown in Bernstein & Khushalani (2000) but moves the coordinates origin to the barycenter (or to the Sun) and assumes a distance and a velocity of the asteroid with respect to this origin. But the high density of tracklets in the (θ_x, θ_y) space (equation 1 in Holman et al. 2018) together with the clustering parameter (equation 11 in Holman et al. 2018) that encloses two distances in a single parameter caused many clusters to mix tracklets that did not belong together.

The third algorithm (and the one we finally used) uses a similar approach to that of HelioLink: assuming the same barycentric distance for all tracklets, clusters were made if the estimated barycentric ecliptic position coincided in two different times (the detailed algorithm is shown in Appendix A and B). Moving the coordinate reference to the solar system barycenter allowed us to cluster tracklets estimating their positions using linear fitting, as seen in Figure 4, where curved trajectories as seen from Earth (left panels) are seen as straight lines (right panels). To cluster as many tracklets as possible it was necessary to try different barycentric distances, although most of them were obtained assuming a distance of 2.5 au (roughly the middle of the Main Belt). With this method we found 1770 asteroids detected in more than 1 night (which highly increased the orbital parameters accuracy, see section 4.1) while using the first method we only found $\lesssim$1100.

To prove that the clustering works properly, we compared the total amount of clustered tracklets with the amount of tracklets that could be obtained from the known asteroids. In Figure 5 we show the number of tracklets per cluster (upper panel) and the time arc per cluster (lower panel) for all found clusters, for all known clusters (tracklets identified as known bodies) and for known clusters as they were actually found by our algorithm (the *recognized* ones), in percentage in each case. Although $\sim$ 70% of tracklets were not linked with any other (clusters of 1 tracklet), the same happened with the known clusters. This, together with the fact that we could link almost all known clusters without contamination (without wrongly joined tracklets), we consider that our linking algorithm worked very well for our data.

4. RESULTS

We produced a total of 5740 tracks after the clustering process. We checked the efficiency of our analysis with the 1422 known objects (Figure 2) that our process could have linked (at least three recognized detections in one night, orange in Figure 3). We found 1323 objects distributed in 1349 tracks. This means we failed to link a minority of related tracklets, yielding a 93% detection efficiency.

4.1. *Orbital Fitting*

As in Peña et al. (2018), we applied a Keplerian orbit fit to each track. Due to the degeneracy in distance and velocity for tracks that span only a few hours we focused only on those that include observations in different nights. We further rejected all trajectories that yield unbound solutions or that deflect more than $2''$ from an observation, leaving 1762 bound trajectories or

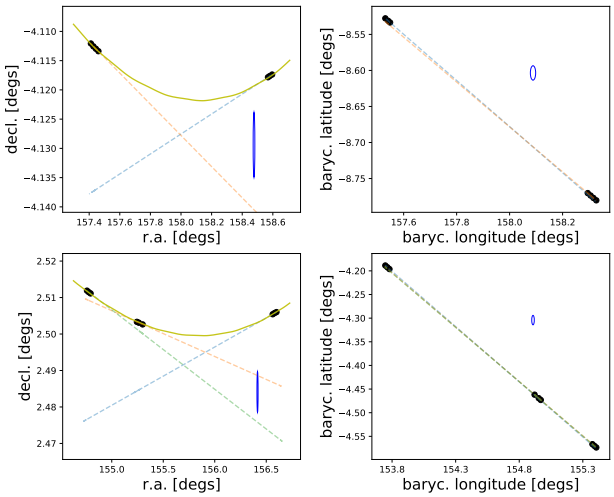

Figure 4. Known asteroids with difficult trajectories. The upper two panels show the asteroid 2009 CP21 and the lower two panels the asteroid 2017 SJ103. On the left, in equatorial coordinates, the HiTS detections (black dots) and the trajectory as estimated by JPL Horizons (yellow line) are shown. On the right we show in black dots the barycentric coordinates as estimated assuming barycentric distances similar to the actual ones. Dashed lines show linear fittings for all tracklets and the blue circles show the maximum distance between estimated coordinates to join these tracklets into tracks (20″ for the first linking algorithm working in equatorial coordinates and 36″ for the last algorithm working in barycentric coordinates).

good tracks from now on. We found 1738 Main Belt asteroids, 6 Near Earth Objects (NEOs) and 4 TNOs as defined in Peña et al. 2018 (See Figure 6).

We estimated our orbital parameter uncertainties using the detection of the 397 known objects with *good tracks* recognized in our sample (see Figure 7). We report our $1-\sigma$ uncertainties as the interval that bounds 68% of the errors around the mode (as in the normal distribution) to be $\sigma_a \sim 0.05$ au for the semi-major axis, $\sigma_e \sim 0.06$ for the eccentricity, $\sigma_i \sim 0.5$ deg for the inclination, $\sigma_r \sim 0.12$ au for the body-barycenter distance and $\sigma_\Delta \sim 0.12$ au for the body-observer distance.

In Figure 8 we can see the distribution of the 1738 bodies identified as Main Belt objects divided in three groups: Inner Belt (from 1.3 to 2.5 au); Middle Belt (from 2.5 to 2.82 au) and Outer Belt (from 2.82 to 4.2 au). The limits between each group are in the most notorious Kirkwood gaps in Figure 8 and have been used to differentiate the MB in different works (such as Parker et al. 2008; Masiero et al. 2011 and DeMeo & Carry 2013, 2014). In each of these populations we found 181, 566 and 991 bodies respectively.

4.2. *Magnitude Distribution*

For each track in our survey we computed a mean magnitude g'. In Figure 9 we show the distribution for all tracks in blue, for those that were recognized

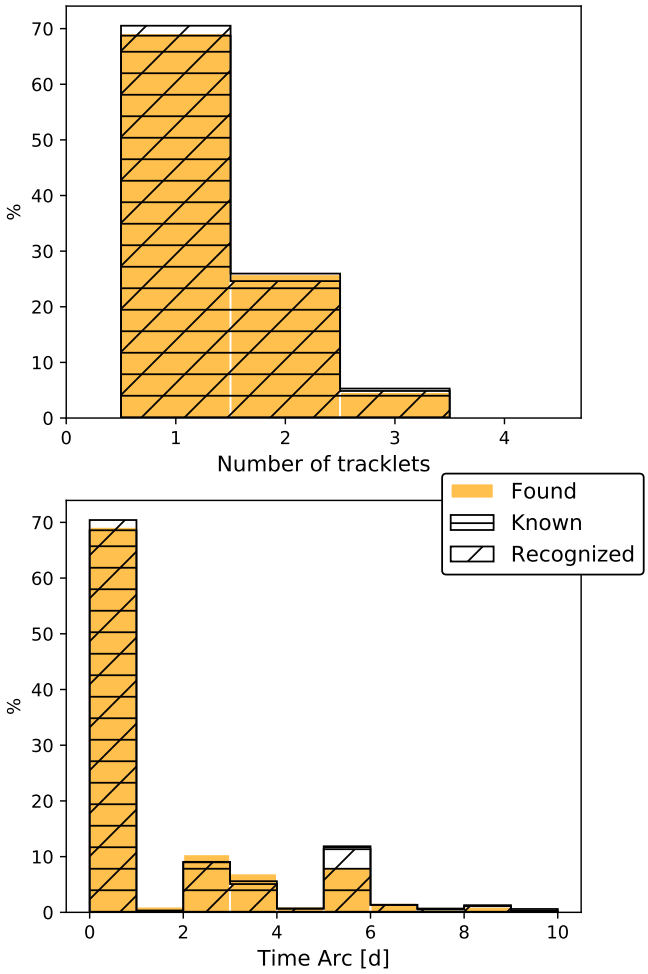

Figure 5. Upper panel: percentage of clusters grouped by their number of tracklets. Lower panel: percentage of clusters grouped by their time arc. In yellow all found clusters are shown, the known ones –if perfectly linked– are shown with horizontal lines, and as actually found with diagonal lines. In total there are 7945 tracklets grouped in 5674 clusters (yellow), 1324 known bodies among those tracklets (horizontal lines) that were found in 1403 clusters (diagonal lines).

as known bodies in green and for all known bodies in orange (regardless of whether they were linked or not).

In Figure 10 we show the luminosity function (LF) in the apparent g' magnitudes for almost all tracks. We left out 37 that showed non-MB orbits considering a criterion similar to that in Yoshida et al. (2003) and Yoshida & Nakamura (2007) (namely, only tracks with MB-like ecliptic velocities of $< -0.15°\text{day}^{-1}$ were included[3]). We expect some contamination among those 5703 track from bodies outside the MB (specially from

[3] Obtained by linearly fitting geocentric ecliptic coordinates using `Python`'s (`https://www.python.org/`) `astropy` package (`https://www.astropy.org/`).

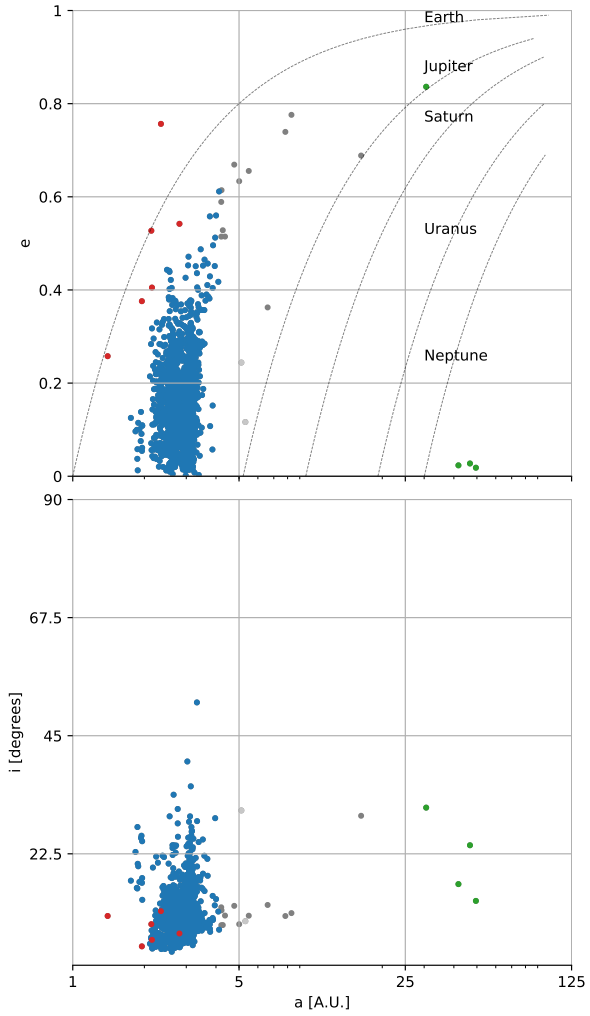

Figure 6. Orbital solution for all tracks detected in at least two nights that yield bound orbits and a maximum deviation of 2″ from the model. There are 1762 objects in 2015 that fulfill this criterion. The lines show the solutions that share their pericenter distance with the outer planets. We show Near Earth Objects in red, Main Belt asteroids in blue, Trans-Neptunian objects in green and others in gray. No Centaurs were found.

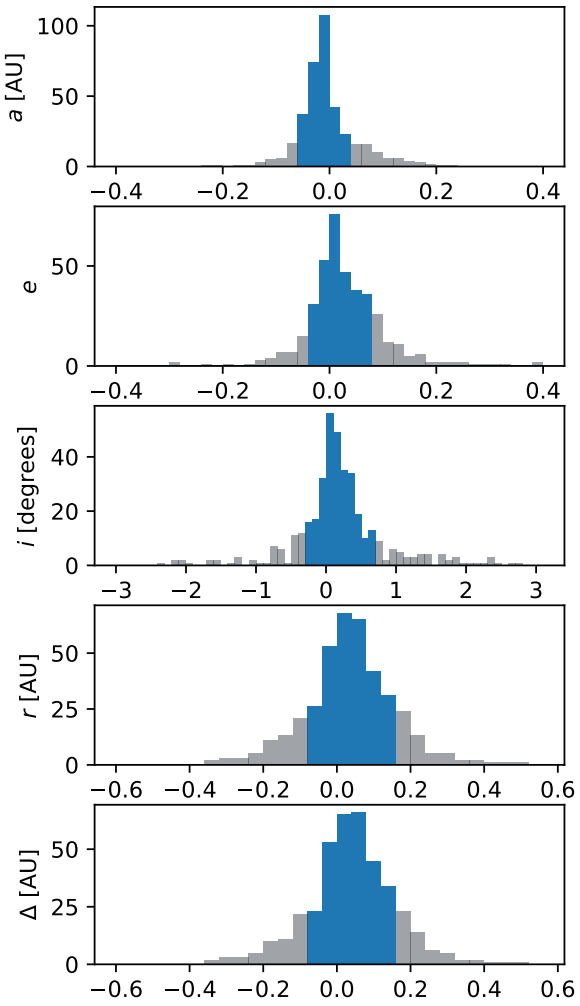

Figure 7. Errors for the estimated orbits of known asteroids in our sample detected in more than one night and with bound computed orbits with fitting errors of $\leq 2''$. We highlight the 1σ confidence region (in blue). From top to bottom we show errors in semi-major axis a, eccentricity e, inclination i, barycenter distance r and observer distance Δ. The implied 1σ confidence region for our orbital solutions is: $\sigma_a = [-0.06, 0.04]$ au, $\sigma_e = [-0.04, 0.08]$, $\sigma_i = [-0.3, 0.7]$ degrees, $\sigma_r = [-0.08, 0.16]$ degrees and $\sigma_\Delta = [-0.08, 0.16]$ degrees.

NEOs), but we do not expect it to be larger than 1%.

The LF exhibits a very clear break that was fit with the harmonic mean of two power laws or double power law (DPL, see equation 1) using the same method shown in Bernstein et al. (2004), Fuentes & Holman (2008) and Fuentes et al. (2009), based on the likelihood function derived by Schechter & Press (1976).

$$\sigma(m) = (1+c)\sigma_{20}\left[10^{-\alpha_1(m-20)} + c10^{-\alpha_2(m-20)}\right]^{-1}$$
$$c = 10^{(\alpha_2-\alpha_1)(m_{eq}-20)} \quad (1)$$

We constrained the LF parameters in equation 1 using Python's package `emcee`[4] (Foreman-Mackey et al. 2013) which applies an affine invariant Markov Chain Monte Carlo (MCMC) ensemble sampler (Goodman & Weare 2010) that returns an approximation of the probability distribution as a function of the models' parameters. We considered a total survey area $\Omega = 138\,\mathrm{deg}^2$ and detection efficiency $\eta(m)$ as in Förster et al. (2016) (equa-

[4] https://emcee.readthedocs.io/

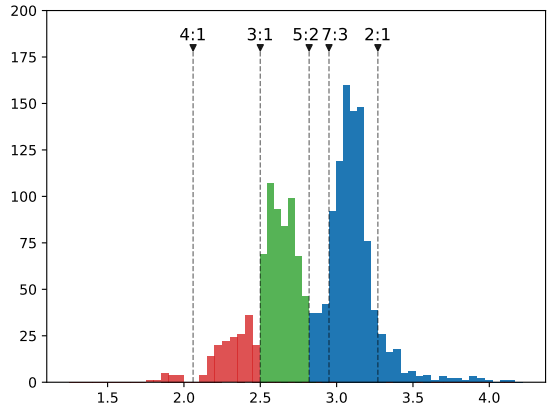

Figure 8. Main Belt distribution as a function of semi-major axis for the 1,738 bodies with *good* orbital solutions (see Figures 7 and 6). Important Kirkwood gaps for resonances 4:1, 3:1, 5:2, 7:3 and 2:1 with Jupiter are plotted in dashed lines, defining the Inner Belt (red), the Intermediate Belt (green) and the Outer Belt (blue), each one with 181, 566 and 991 bodies, respectively.

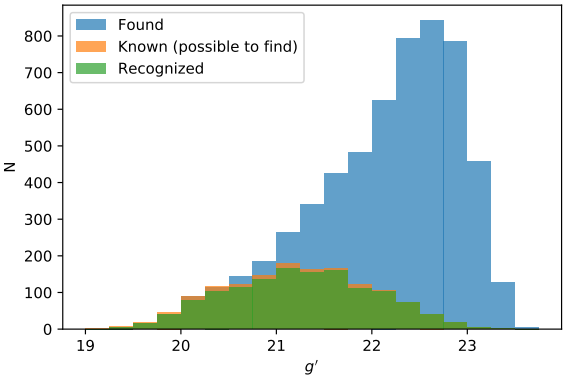

Figure 9. Histograms of the number of asteroids per magnitude (g' band). In orange, known asteroids (from JPL) that our linking process can find (wich haveat least three detections in any night). In blue, tracks found in the HiTS data. In green, those tracks that were recognized as known objects (at least three detections within 4″ of a JPL detection). The drop in the blue histogram appears consistent with Figure 7 in Förster et al. (2016) once the effect of image subtraction is taken into account, which results in a loss of ∼0.4 mag.

tion 2, with erf the error function[5]). Taking into account image subtraction and multiple detections yields parameters $m_{50} = 23$ and $\Delta m_{50} = 1.1$ for the detection efficiency function of asteroids.

$$\eta(m) = \frac{1}{2}\left[1 + \mathrm{erf}\left(-\frac{m - m_{50}}{\Delta m_{50}}\right)\right] \quad (2)$$

We considered $\eta(m)$ and detections up to the limiting

[5] $\mathrm{erf}(x) = \frac{2}{\pi}\int_0^x e^{-t^2} dt$

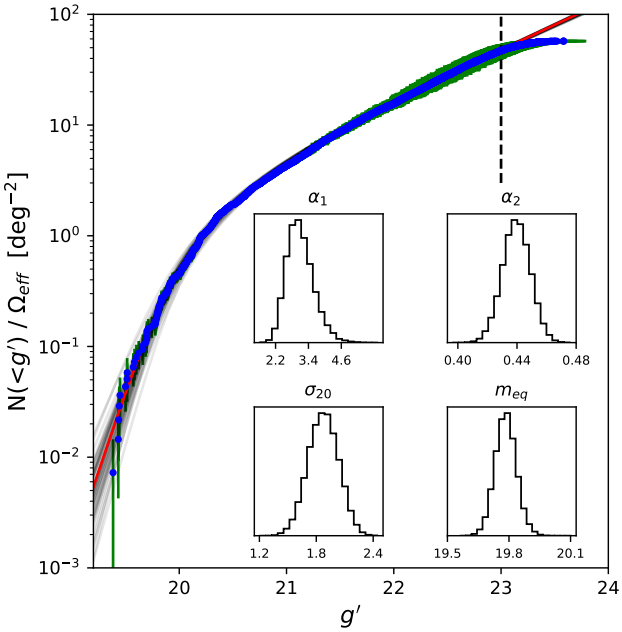

Figure 10. Cumulative distribution of magnitude g' for the 5703 tracks with MB-like velocities (see section 4.2). A DPL (equation 1) was fitted using MCMC to the 5119 bodies brighter than 23 g' (marked with a dashed line). The small panels show the DPL parameters distribution. Using the mode with a ±34% confidence interval, we got $\alpha_1 = 2.94^{+0.48}_{-0.48}$, $\alpha_2 = 0.44^{+0.01}_{-0.01}$, $\sigma_{20} = 1.86^{+0.22}_{-0.15}$ and $m_{eq} = 19.78^{+0.06}_{-0.06}$. The red line shows the DPL given by the median values and the gray lines show 50 random models from the MCMC procedure.

magnitude of our survey ($g' \sim 23$), limiting our sample to 5119 objects. Each of the 200 walkers used for this algorithm started at a random position near the parameter value obtained using the common χ^2 minimization method. Using the mode with a ±34% confidence interval, we finally got $\alpha_1 = 2.94^{+0.48}_{-0.48}$, $\alpha_2 = 0.44^{+0.01}_{-0.01}$, $\sigma_{20} = 1.86^{+0.22}_{-0.15}$ and $m_{eq} = 19.78^{+0.06}_{-0.06}$.

This LF is very similar to that found by Gladman et al. (2009), with a break at $R \sim 19$, consistent with our $m_{eq} \sim 19.78$ (our mean color $g' - r' \sim 0.77$, see Table 3). They got flatter slopes, especially at the bright end: $\alpha = 0.61$ compared to our much steeper $\alpha_1 \sim 3.1$; while at the faint end they got $\alpha = 0.27$ against our $\alpha_2 = 0.44$. The expected number of bodies is also lower for our survey: Gladman et al. (2009) found ∼ 90 bodies per square degree brighter than $R \sim 22$, while we only found ∼ 30 bodies brighter than $g' \sim 22.7$. This is accounted by the fact that they pointed directly at the ecliptic while in this work the area closest to the ecliptic is at ∼ 8° with the bulk of our data is at ∼ 15°. This is consistent with the results by Ryan et al. (2009), who showed that the number of detected asteroids decreases with ecliptic latitude by 50% and 20% at 10° and 15° with respect to 0°.

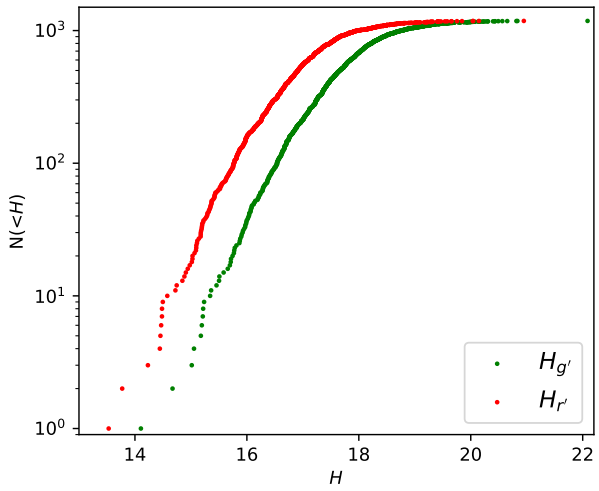

Figure 11. Cumulative distribution of $H_{g'}$ and $H_{r'}$ for the 1182 MB bodies with *good* orbital solution and measurements in g' and r' bands.

4.3. *Absolute Magnitude Distribution*

We computed absolute magnitudes H for all *good tracks*. In equation 3 r is the body-barycenter distance, Δ is the body-observer distance, α is the phase (Sun-body-observer angle), and $\phi(\alpha)$ is the phase function (see Waszczak et al. 2015 for several definitions of ϕ). We used the (H, G) model for ϕ (Bowell et al. 1989), using the typical value of $G = 0.15$ (as in the ephemeris data delivered by MPC and JPL). Since we had data mainly in g' and some in r', we computed the absolute magnitudes for each filter, $H_{g'}$ and $H_{r'}$. We report the average absolute magnitude for a track.

$$H = V - 5\log_{10}(r\Delta) + 2.5\log_{10}[\phi(\alpha)] \quad (3)$$

Since H can be related with the body's size by the equation $D = 10^{-H/5}1329/\sqrt{p_V}$, where D is the diameter in km and p_V the geometric albedo, we sought for a possible color–size relation in the MB using H as a proxy for the size (assuming a common p_V for all bodies). In Figure 11 we show the cumulative *size* distribution (CSD) for the 1182 MB bodies measured in g' and r' bands. Both $H_{g'}$ and $H_{r'}$ distributions are well represented by a single power law (SPL) with the same slope (~ 0.88), showing no evidence for any color–size relationship in our data. This result was unchanged even when we considered each MB zone separately (Inner, Middle and Outer).

In the following analysis we only considered $H_{g'}$ since all tracks were observed in g'. Following the process described in section 4.2, we fit an SPL distribution $\sigma = \alpha \ln(10) 10^{\alpha(mag-H_0)}$ using only bodies brighter than our limiting magnitude ($g' \sim 23$). The SDs are shown in Figure 12 and the most likely parameters are summarized in Table 2. The MB as a whole or by sub-region exhibits slopes much steeper than measured by other studies, only comparable to the ones measured by Parker et al. (2008) for brighter objects.

Since DECam has similar filters to those in SDSS (Schlafly et al. 2018), we used Lupton (2005)[6] to transform $H_{g'}$ to H (g' to V). Lupton found that $V \sim g' - 0.58(g' - r')$ (similar to the results found by Fukugita et al. 1996 and Krisciunas et al. 1998). Assuming all bodies have the same color and albedo, $g' - r' \sim 0.76$ (see section 4.4), and $p_V = 0.1$ (roughly the mean albedo from Polishook et al. 2012), sizes range between $1 < D < 10$ km for objects between $14 < H_{g'} < 18$.

Table 2. Main Belt SPL fitting

Population[a]	H_{lim}[b]	N[c]	α[d]	H_0[d]
Main Belt	16.56	129	$0.88^{+0.09}_{-0.08}$	$16.04^{+0.09}_{-0.05}$
Inner Belt	18.4	57	$0.76^{+0.13}_{-0.10}$	$18.28^{+0.09}_{-0.09}$
Intermediate Belt	17.7	173	$0.79^{+0.06}_{-0.06}$	$16.96^{+0.1}_{-0.07}$
Outer Belt	16.56	108	$0.86^{+0.12}_{-0.08}$	$16.14^{+0.09}_{-0.06}$

[a] As defined in Section 4.1.

[b] Limiting $H_{g'}$ magnitude for fitting.

[c] Number of bodies brighter than H_{lim}.

[d] Values are the median with a confidence interval of ±34% from the distribution.

4.4. *Color*

The 2015A HiTS campaign observed in both g' and r', but most revisits were in g', enabling us to detect tracks in both filters and produce colors for some of our tracks. We report $g' - r'$ colors from $H_{g'} - H_{r'}$ (section 4.3) for the 1203 *good tracks* measured in both bands. In Figure 13 we show these colors for the 1182 located in the region of the Main Belt as a function of their orbital parameters and in Figure 14 the $g' - r'$ distribution in the entire Main Belt is shown separated by class: Inner, Intermediate and Outer Belt. In both figures we observe that asteroids are mainly red, with a mean color of $g' - r' \sim 0.756 \pm 0.008$ for all of them. Although we could not recognize any color–size dependency (section 4.3), we recovered the known color-distance relationship (Yoshida & Nakamura 2007; Gladman et al. 2009), as seen in Figure 14. Summarized in Table 3 we show that MB asteroids get bluer as they get farther

[6] http://classic.sdss.org/dr7/algorithms/sdssUBVRITransform.html

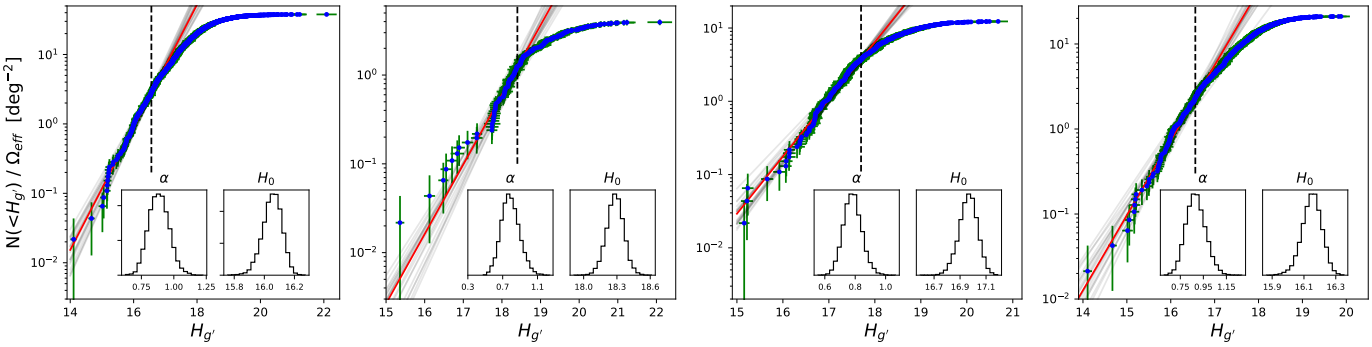

Figure 12. Cumulative H distribution of bodies with good orbital solutions for (a) all MB bodies; (b) inner MB bodies; (c) intermediate MB bodies; and (d) outer MB bodies. A single power–law distribution was fit ($\sigma(H_{g'}) = \alpha \ln(10) 10^{\alpha(H_{g'} - H_0)}$), with the two smaller panels showing the parameter distribution. In red we show the model given by the median values and in gray models given by 20 random values from the parameter distributions. Dashed lines mark the limiting magnitude (only brighter bodies are considered for the fit). A summary of the fitting results is in Table 2.

from the Sun. This dependency is usually explained as an asteroid type dependency: the outer belt would be dominated by C-type asteroids (bluer) and the inner belt would be dominated by S-type (redder); (as seen in many color plots; e.g., Ivezić et al. 2001; Yoshida & Nakamura 2007; Gladman et al. 2009). If we use Ivezić et al. (2001) as a reference, the $g' - r'$ limit between C– and S–types would be around ~ 0.55, meaning that the vast majority of our asteroids would be S-type in the three MB divisions. We were not able, however, to distinguish any clear bimodality as in Ivezić et al. (2001) to distinguish between types.

We explain the lack of the expected bimodality in color taking into account the asteroids' intrinsic lightcurves due to rotation. Most asteroids exhibit some variation with periods that range from ∼2 hours to ∼2.5 days (remember our 1.6 hour cadence), changing their brightness by 0.1 to 1.2 magnitudes (Polishook et al. 2012; Waszczak et al. 2015). Another posible contaminating source in our sample are NEOs, which exhibit similar rotational periods (Vaduvescu et al. 2017). Our reported colors were measured as the average $H_{g'}$ (several values) minus the average $H_{r'}$, the latter generally being only one value measured at ∼1.6 hours from the nearest g' measure. This means that colors reported in this work have a big uncertainty due to asteroid's rotation. In comparison, SDSS colors are measured within ~ 5 minutes Ivezić et al. (2001). WISE, for example, observed in 4 bands simultaneously (Wright et al. 2010) allowing the measurement of p_V for bodies with accurate orbital parameters and obtaining a strong bimodality associated with composition (Masiero et al. 2011).

Table 3. $g' - r'$ colors for the Main Belt

Population[a]	N[b]	Mean	Stand. Dev.
Main Belt	1182	$0.756 \pm .008$	$0.181 \pm .008$
Inner Belt	133	$0.797 \pm .031$	$0.175 \pm .033$
Intermediate Belt	369	$0.776 \pm .015$	$0.186 \pm .015$
Outer Belt	680	$0.737 \pm .010$	$0.177 \pm .010$

[a] As defined in Section 4.1.

[b] Number of bodies in each population.

NOTE—The errors in the last two columns are computed taking into account the magnitudes errors and the confidence intervals shown in Section 4.1 (Figure 7).

Outside the Main Belt, we obtained colors for 12 known objects: 5 NEOs, 3 TNOs and 4 Jupiter family comets (JFCs). Colors for these bodies can be seen in Table 4. NEOs have colors somewhat bluer than the MB's average color, which is consistent with Dandy et al. (2003), who claim the MB as a possible source, finding NEOs bluer than expected. The 4 JFCs are redder than the mean color of the MB, but inside the MB color range as seen in Solontoi et al. (2012) (in $g' - r'$, with Ivezić et al. 2001 and this work for comparison) or in Lamy & Toth (2009) and Jewitt (2015) (in $B - R$, with Yoshida & Nakamura 2007 for comparison). For the TNOs, following the classification algorithm defined by Gladman et al. (2008) and using the limit for scattered objects by Lykawka & Mukai (2007), (531017) 2012 BA_{155} is a 2:5 resonant body, 2014 XW_{40} is a scattered TNO and (523671) 2013 FZ_{27} is in the limit between scattered and hot, outer classical TNO (and is also near the detached TNO zone). These 3 TNOs have red colors compati-

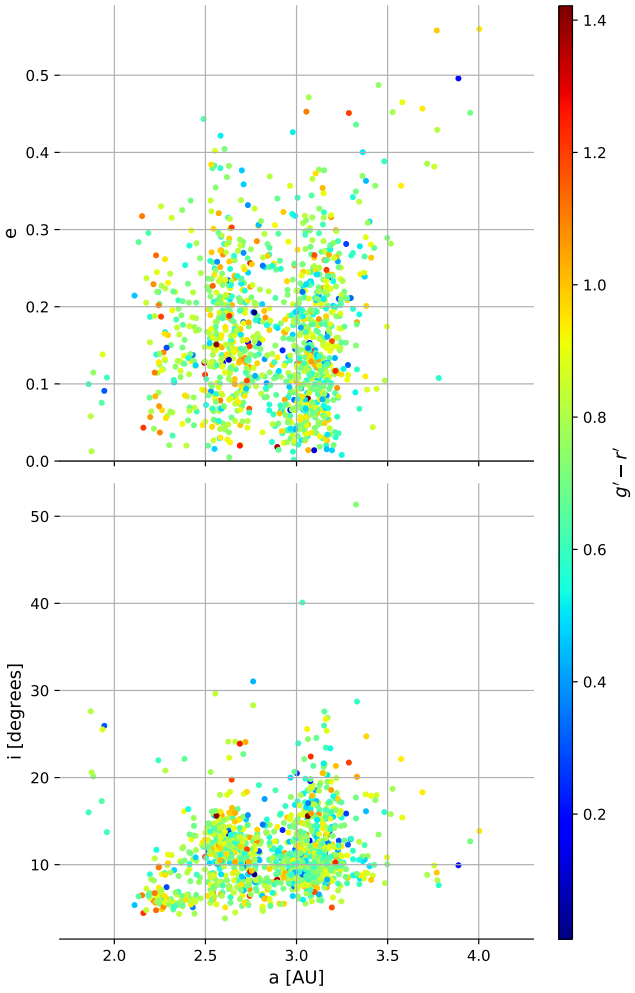

Figure 13. Same as Figure 6 but for Main Belt objects only that were also measured in r with their respective $g' - r'$ color (measured from their $H_{g'}$ and $H_{r'}$ values).

ble with their respective families (Sheppard 2010; Jewitt 2015; Pike et al. 2017; Terai et al. 2018).

Table 4. $g' - r'$ colors for Non Main Belt known bodies

Name[a]	Type [b]	$g' - r'$ [c]	$H_{g'}$
2003 HU42	NEO	0.67 ± 0.20	18.00 ± 0.01
2008 VU4	NEO	0.75 ± 0.18	18.04 ± 0.05
2003 SS214	NEO	0.60 ± 0.16	20.14 ± 0.06
2014 WL368	NEO	0.85 ± 0.05	20.19 ± 0.04
2017 JB	NEO	0.47 ± 0.12	23.66 ± 0.08
C/2015 D2	JFC	0.80 ± 0.04	13.29 ± 0.02
P/2011 U2	JFC	1.064 ± 0.030	13.96 ± 0.01
C/2014 A5	JFC	0.87 ± 0.10	15.43 ± 0.04

Table 4 continued

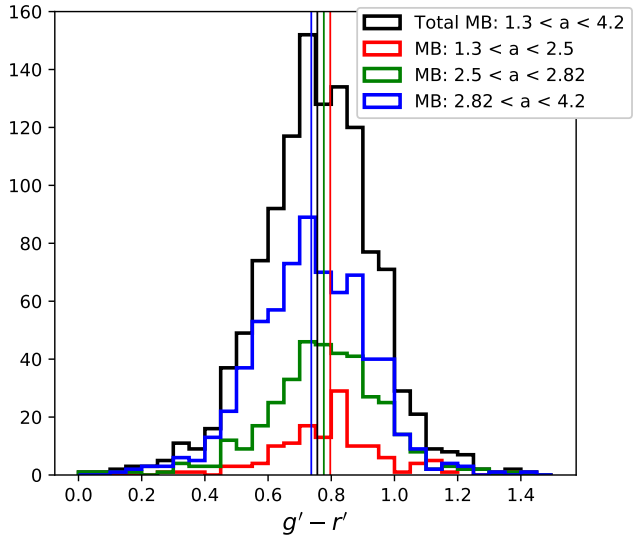

Figure 14. Histograms of the color of Main Belt asteroids. In black: all Main Belt asteroids; in red: Inner Belt; in green: Intermediate Belt; and in blue: Outer Main asteroids. Vertical lines mark the mean color for each population (see Table 3). Notice that the average $g' - r'$ colors for C and S asteroids (based in Ivezić et al. 2001) are 0.45 and 0.65 respectively.

Table 4 *(continued)*

Name[a]	Type [b]	$g' - r'$ [c]	$H_{g'}$
317P/WISE	JFC	0.79 ± 0.08	18.93 ± 0.07
2013 FZ27	TNO	0.92 ± 0.05	4.72 ± 0.02
2012 BA155	TNO	1.17 ± 0.15	6.57 ± 0.10
2014 XW40	TNO	1.25 ± 0.13	6.79 ± 0.07

[a] As identified by the MPC and JPL

[b] NEO: Near Earth Object; JFC: Jupiter Family Comet (as identified by the JPL Small-Body Database Browser); TNO: Trans-Neptunian Object

[c] Colors computed as the difference of the averaged $H_{g'}$ and $H_{r'}$. The errors only consider magnitude uncertainty. To calculate H we use orbital data (r and Δ) from JPL Horizons.

5. SUMMARY AND DISCUSSION

Using data from the HiTS 2015 campaign, we found 5740 SS minor bodies. Considering only bodies with an observation arc longer than one night, we were able to identify 1738 MB asteroids (397 of them were known bodies), getting color information for 1182 of them.

The luminosity function for all bodies with apparent motions compatible with MB bodies (5703 in total) is well fit by a DPL, similar to the one found by Gladman et al. (2009), with a break in a similar magnitude but

with much steeper slopes.

We found the size distribution for the MB population compatible with a SPL for the entire population as well as for the Inner, Intermediate and Outer MB separately. The slope parameters for these populations are much higher than previous surveys have reported, only comparable with values found by Parker et al. (2008) at the bright end of the distribution.

We did not find a color–size dependence between 14 $< H_{g'} <$ 18 ($1 < D <$ 10 km), as previously reported by August & Wiegert (2013) for similar sizes (analyzing over 7,000 bodies). Ivezić et al. (2001) could not find a color–size relationship for similar objects analyzing ∼670,000 bodies in multiple filters.

The colors we report are most similar to S-type bodies in the MB, which is compatible with the scenario of the Outer MB (the most populous region of the MB) is dominated by S-type asteroids. We could not find any bimodality in color. In order to explain this we simulated an intrinsic bimodal population like the one by Ivezić et al. (2001) (top panel of Figure 15). To measure how asteroids' rotation affects the measured color, we modeled their magnitudes as $m = m_0 + A\sin(2\pi(\phi + f\Delta t))$ with m the measured value, m_0 the mean magnitude (pseudo-randomly generated with equation 1 as a probability distribution), A the magnitude variation (obtained from a pseudo-random triangular distribution between 0 and 1.2 magnitudes with the mode at 0.2), f the rotation's frequency (obtained from a pseudo-random triangular distribution between 0.5 and 10 days^{-1} with the mode at 0.5), ϕ the phase of the first observation (obtained from a pseudo-random flat distribution) and Δt the time between one observation and another ($\Delta t = 0$ for the simulated first observation and $\Delta t = 1.6$ hours for the second observation in the HiTS 2015 case). The A and f distributions are based on Waszczak et al. (2015). Finally, the apparent color $g' - r'$ we obtained (with g' obtained as m_0 and r' as $m(\Delta t = 1.6h)$) is shown in the lower panel of Figure 15, where the color distribution has broadened and lost any bimodality. We further estimated the effect of a time lag between filters on colors due to an asteroid's rotation. In Figure 16 we show the standard deviation of the errors between consecutive measurements of our simulated population ($\sigma(\Delta_{g'-r'})$) as a function of the time between those observations; since the two modes of our *"true"* color distribution (top panel in Figure 15) are 0.2 magnitudes apart, we set a rough $\sigma(\Delta_{g'-r'})$ limit of at least 0.1 to detect the bimodality. This value is found at $\Delta t = 0.24$ hours or ∼ 14 minutes (red lines in Figure 16). This is an important constraint for future surveys such as LSST (LSST Science Collaboration et al. 2009), which plans to visit one sky field twice a night, taking two images per visit. Since visits can be a few hours apart, ideally

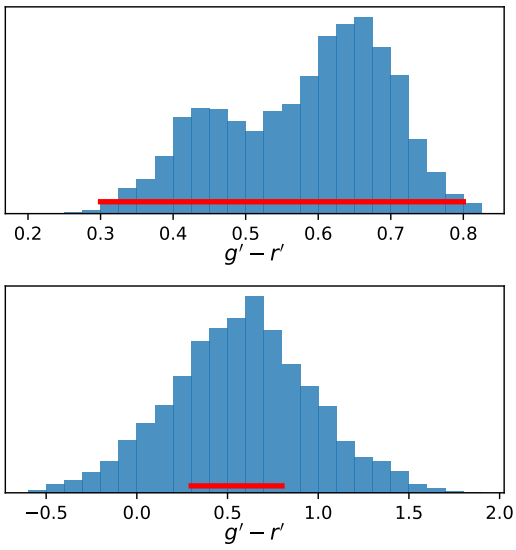

Figure 15. Top panel: simulated color bimodality resembling the one seen in Ivezić et al. (2001). Lower panel: apparent color due asteroids' rotation (see text). In both panels, the red line covers the same range, showing how the apparent color distribution gets wider because asteroids' rotation.

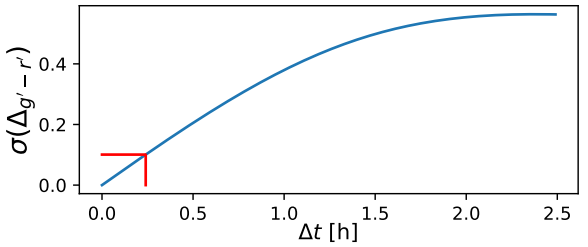

Figure 16. Standard deviation of the errors in color using consecutive measurements $\sigma(\Delta_{g'-r'})$ of the simulated population (see Figure 15) vs. time between observations Δt. In red we indicate the time separation $\Delta t = 0.24$hr that yields an uncertainty $\sigma(\Delta_{g'-r'}) = 0.1$ small enough to detect bimodality in the color distribution (see text).

the two images per visit should be in different filters to retrieve good colors. Although LSST will deliver large lightcurves for many asteroids, allowing to measure colors even if the two images per visit were in the same filter (Ivezić et al. 2018), this will be possible only for asteroids well tracked through many nights for a long time, while if the color is measured per visit we would be able to have colors for nightly tracklets even for those cases when the body is detected only once (generally the case for small bodies at the limiting magnitude).

The slopes we got in our size distributions are much steeper than in any other survey, only comparable to the ones found by Parker et al. (2008) for bright bodies. Our lower surface density of detections is consistent with Gladman et al. (2009) if we take into consideration the

amount of asteroids by ecliptic latitude found by Ryan et al. (2009), so our steep values would be caused by a lack of bright bodies (less numerous but able to flatten the distribution). The apparent lack of bright bodies could be an effect of the ecliptic latitudinal distribution of asteroids on the observed luminosity function or it could be an effect of the analysis of HiTS moving objects. The *deep learning* analysis that distinguishes between real and bogus detections was designed for static (not elongated) transients and not specifically for moving objects, but there is no reason to believe it would discriminate bright bodies worst than faint bodies.

We explored the latitudinal dependence by analyzing the SD of asteroids from the HiTS 2014 campaign (Peña et al. 2018). Those asteroids were found mainly between ecliptic latitudes 0° and 15°. Using bodies with an apparent ecliptic latitude velocity compatible with the MB (less than $-0.16°\text{day}^{-1}$ instead of less than $-0.15°\text{day}^{-1}$ as for the 2015 data because in 2014 campaign we have Jupiter trojans around $-0.15°\text{day}^{-1}$) and following the same procedure as in Section 4.2 (using $m_{50} = 23.6$ and Δm_{50}=1.1 for η in equation 2 and $\Omega = 120\text{deg}^2$ for the surveyed area) we obtained the distribution shown in Figure 17, which exhibits a slope of ~ 0.76 for the bright end and a slope of $\sim .28$ for the faint end. These values are very similar to (although somewhat steeper than) the values found by Gladman et al. 2009 (see dashed lines from Figure 17). Continuing the analysis of the 2014 data, we computed the SD for all "*good*" tracks (using the same criteria from Section 4.1) and fitted a DPL to it (an SPL was not enough to fit the data). This DPL has the same form as equation 1, but instead of using magnitude 20 as reference, we used magnitude 16. The result is shown in Figure 18, where the DPL was fitted using data up to a limiting magnitude $H_{g'} = 17.18$ (using a limiting magnitude of $g' = 22.5$ for 90% completeness and a phase angle of less than 9.2°). The resulting slopes are $0.68^{+0.17}_{-0.09}$ at the bright end and $0.34^{+0.04}_{-0.11}$ at the faint end, which is consistent with previous results such as Ivezić et al. (2001) and Gladman et al. (2009). This supports the hypothesis that the steeper slopes for our 2015 campaign are due to a lack of bright sources at higher latitudes. A similar result was found by Bhattacharya et al. (2010), where bodies at latitude $\sim 5°$ have fluxes 30% fainter than those at latitude $\sim 0°$. We will further investigate the effect of this latitudinal distribution of asteroids on the observed luminosity function and the apparent lack of bright bodies in our survey.

HiTS as a high cadence survey was a precursor of wider future surveys such as the LSST. Although it was not optimized specifically for finding asteroids, its wide coverage and high cadence ~~of HiTS~~ proved to be appropriate for discovering asteroids. We found that having at least three observations of the same field in a night (*tracklet*) is important for this task. Fitting an accurate orbit for a new discovery requires observations in at least two nights, which for the sparse sky coverage of HiTS is more likely if the same field is visited in consecutive nights while objects are still there. LSST will visit the same sky ~ 3 nights later, improving the orbit estimation but hindering the pairing of *tracklets* between nights. Another important quality of HiTS is its machine learning vetting algorithm that discriminates true sources from bogus; this speeds up the linking of asteroids and diminishes the probability of mixing unrelated detections. Finally, HiTS cadence, although excellent for asteroids discovery, is not well suited for color measurements due to asteroid rotation. Surveys should plan on taking consecutive multifilter observations for accurate color measurements whenever observing conditions are photometric.

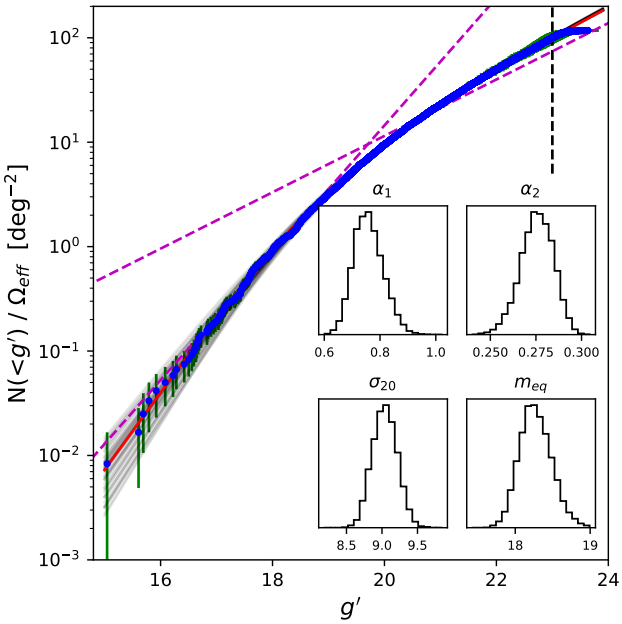

Figure 17. Cumulative distribution of magnitude g' for the 12,928 tracks with MB-like velocities from the 2014 HiTS campaign (see section 5). A DPL was fit using MCMC to the 11,419 bodies brighter than 23 g' (marked with a black dashed line). The small panels show the DPL parameter distributions. Using the mode with a ±34% confidence interval, we got $\alpha_1 = 0.76^{+0.05}_{-0.06}$, $\alpha_2 = 0.28^{+0.01}_{-0.01}$, $\sigma_{20} = 9.03^{+0.18}_{-0.18}$ and $m_{eq} = 18.16^{+0.33}_{-0.11}$. The red line shows the DPL given by the mode values and the gray lines show 50 random models from the MCMC procedure. In magenta dashed lines there is a proxy of the distribution by Gladman et al. (2009), considering they found ~ 100 bodies at $R \sim 19.1$ at the bright end (slope of 0.61), ~ 1000 bodies at $R \sim 23$ at the faint end (slope of 0.27), $\Omega = 8.4\text{deg}^2$ and approximating $g - R \sim 0.76$ (from Section 4.4).

6. ACKNOWLEDGMENTS

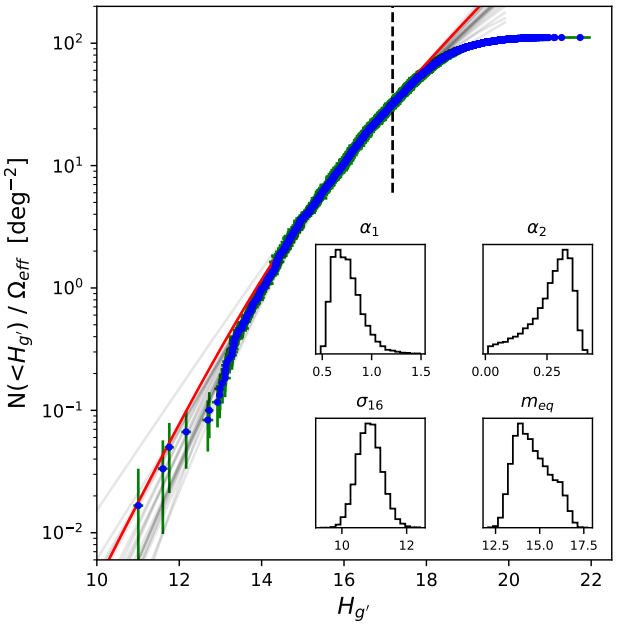

Figure 18. Cumulative H distribution for all 6679 MB bodies with good orbital solutions from the 2014 HiTS campaign (following the same criteria as for the 2015 HiTS campaign). A DPL (see text) was fit using MCMC to the 1729 bodies brighter than $H_{g'} = 17.06$ (marked with a dashed line). The small panels show the DPL parameter distributions. Using the mode with a ±34% confidence interval, we got $\alpha_1 = 0.68^{+0.17}_{-0.09}$, $\alpha_2 = 0.34^{+0.04}_{-0.11}$, $\sigma_{16} = 10.85^{+0.40}_{-0.40}$ and $m_{eq} = 13.82^{+1.63}_{-0.51}$. The red line shows the DPL given by the mode values and the gray lines show 20 random models from the MCMC procedure.

J.P. acknowledges the support from CONICYT Chile through (CONICYT-PFCHA / Doctorado-Nacional / 2017-21171752). J.P., C.F., F.F., J.S.M., G.C.V., S.G.G. and J.M. acknowledge support from Grant PIA AFB-170001, Centro de Modelamiento Matemático (CMM), Universidad de Chile. F.F., M.H., S.G.G., P.A.E., G.C.V., and J.M. acknowledge support from the Ministry of Economy, Development, and Tourisms Millennium Science Initiative through grant IC120009, awarded to The Millennium Institute of Astrophysics (MAS). J.P., C.F. acknowledge support from the BASAL Centro de Astrofísica y Tecnologías Afines (CATA) PFB-06/2007. F.F. acknowledges support from Conicyt through the Fondecyt Initiation into Research project No. 11130228. S.G.G. and L.G. acknowledge support from FONDECYT postdoctoral grants 3130680 and 3140566, respectively. G.C.V. acknowledges support from CONICYT through the FONDECYT Initiation grant No. 11191130 P.A.E. and P.H. acknowledge support from FONDECYT regular grants 1171678 and 1170305, respectively. L.G. was funded by the European Union's Horizon 2020 research and innovation programme under the Marie Skłodowska–Curie grant agreement No. 839090. S.G.G. acknowledges support of FCT under Project CRISP PTDC/FIS-AST-31546. J.M. acknowledges the support from CONICYT Chile through CONICYT-PFCHA/Doctorado-Nacional/2014-21140892. TdJ was funded by the Bengier Postdoctoral Fellowship and is grateful to Gary and Cynthia Bengier for their support. Powered@NLHPC: this research was partially supported by the supercomputing infrastructure of the NLHPC (ECM-02). Part of this work was done under the Harvard-Chile data science school. This project used data obtained with the Dark Energy Camera (DECam), which was constructed by the Dark Energy Survey (DES) collaboration. Funding for the DES Projects has been provided by the U.S. Department of Energy, the U.S. National Science Foundation, the Ministry of Science and Education of Spain, the Science and Technology Facilities Council of the United Kingdom, the Higher Education Funding Council for England, the National Center for Supercomputing Applications at the University of Illinois at Urbana–Champaign, the Kavli Institute of Cosmological Physics at the University of Chicago, Center for Cosmology and Astro–Particle Physics at the Ohio State University, the Mitchell Institute for Fundamental Physics and Astronomy at Texas A&M University, Financiadora de Estudos e Projetos, Fundação Carlos Chagas Filho de Amparo, Financiadora de Estudos e Projetos, Fundação Carlos Chagas Filho de Amparo à Pesquisa do Estado do Rio de Janeiro, Conselho Nacional de Desenvolvimento Científico e Tecnológico and the Ministério da Ciência, Tecnologia e Inovação, the Deutsche Forschungsgemeinschaft and the Collaborating Institutions in the Dark Energy Survey. The Collaborating Institutions are Argonne National Laboratory, the University of California at Santa Cruz, the University of Cambridge, Centro de Investigaciones Energéticas, Medioambientales y Tecnológicas–Madrid, the University of Chicago, University College London, the DES–Brazil Consortium, the University of Edinburgh, the Eidgenössische Technische Hochschule (ETH) Zürich, Fermi National Accelerator Laboratory, the University of Illinois at Urbana–Champaign, the Institut de Ciències de l'Espai (IEEC/CSIC), the Institut de Física d'Altes Energies, Lawrence Berkeley National Laboratory, the Ludwig–Maximilians Universität München and the associated Excellence Cluster Universe, the University of Michigan, the National Optical Astronomy Observatory, the University of Nottingham, the Ohio State University, the University of Pennsylvania, the University of Portsmouth, SLAC National Accelerator Laboratory, Stanford University, the University of Sussex, and Texas A&M University.

APPENDIX

A. TRANSFORMING OBSERVER'S COORDINATES TO BARYCENTRIC COORDINATES

Making *tracklets* (collections of detections that resemble a linear trajectory) is easy if you consider detections of only one night, but to link detections from one night to another proves to be challenging (linear fitting does not work all the times and we do not always find a body every night). To solve this, we decided to change our coordinate reference to the barycenter of our solar system, where the coordinates of our tracklets should resemble straight lines and linear extrapolation to join different bodies would easily work. The problem is that to do this we needed to know the distance of these bodies to the observer's position or to the barycenter. This meant that we had to assume different distances to look for linear trajectories in the barycentric frame.

Assuming that all detections are at distance r to the barycenter, we needed to know the position of the Earth in the barycentric frame ($\mathbf{r_E}$) to solve all the geometry. To make the transformations from the observer's frame to the barycentric frame we used the module `SkyCoord` from the `astropy` package (Astropy Collaboration 2013, 2018) of `Python`. To do this, having the equatorial coordinates of the bodies as seen by the observer together with the observer's position we needed to measure the distance Δ between the observer and the bodies. Using trigonometry, it is easy to see that Δ is given by equation A2 (solving the quadratic equation given by Equation (A1)[7]), where ϕ is the elongation (angle between the body and the barycenter)[8].

$$r^2 = r_E^2 + \Delta^2 - 2 r_E \Delta \cos\phi \tag{A1}$$

$$\Delta = r_E \cos\phi + \sqrt{r_E^2 \cos^2\phi - r_E^2 + r^2} \tag{A2}$$

Having the equatorial coordinates from the observer, the observer's position $\mathbf{r_E}$ and the distance from the observer to the body Δ, it is possible to move the origin of the body's coordinates to the barycenter. An example of the kind of equations you need for this are in Bernstein & Khushalani (2000). To make this transformation, we used the simple interface facilitated by `python`'s `astropy.SkyCoord` (along with other `astropy`'s functionality such as "`time`", "`units`", etc). The frame we used is that of the barycentric ecliptic coordinates.

B. NIGHT–TO–NIGHT LINKING ALGORITHM

Once we had the barycentric ecliptic coordinates for all tracklets (assuming a body-observer distance r), we estimated their position at two different times using a linear fitting on their coordinates. This fit used the corrected time t' approximated by $t' = t - 1/c$, where t is the observed time for each coordinate and c the speed of light.

For each of the estimated times, we performed a neighbor finding routine using a k-d tree algorithm[9] on their estimated coordinates to associate a tracklet to others if their estimated positions were close enough. To cluster one tracklet tr_j to other tracklets ($\{tr_i\}_{i\neq j}$) we took care that in $\{tr_i\}_{i\neq j}$ there were no tracklets from the same night as tr_j. This did not stop $\{tr_i\}_{i\neq j}$ from having tracklets in the same night. To manage this problem, we divided the cluster $\{tr_j \cup \{tr_i\}_{i\neq j}\}$ into as many clusters as necessary so there were no repeated nights in any of the final clusters. Having done this clustering in both times independently, we crossed both sets of clusters to end with a collection where every clustered tracklets must have been clustered in both estimated times. We called any of this final clusters *tracks*.

The times for the estimated positions were chosen to fall at roughly one and three quarters of the total arc of this survey (57,073 and 57,077 in modified Julian dates). The radius to make the clustering was based on the necessary radius to cluster most of the known bodies that were found among the tracklets without joining tracklets that did not correspond to the known asteroids. The radius that optimized both criteria was found to be 0.01 degrees. Using other radii (namely, getting more tracks in only one night or mixing tracklets that were not the same body) increased the error when estimating orbital parameters (see section 4.1).

Since we split clusters so they all were from different nights we could end up with tracklets repeated in more than one cluster. For these cases, we repeated the coordinate estimation process but used estimation times falling at 1/4

[7] You could be tempted to replace $r_E^2 \cos^2\phi - r_E^2$ by $r_E^2 \sin^2\phi$ but if you are using `Python`'s `numpy` it will give you large errors for Δ.

[8] `astropy` easily allows us to know the Sun's position seen by the observer, which is corrected by the light's travel time. That is *not* the position we want, but the actual one at observing time. We managed to get this last one by using the observer's position delivered by `astropy.coordinates.EarthLocation` ($\mathbf{r_E}$) transformed to the barycentric frame and then inverting the sign of their cartesian values to get the Sun's position in the observer's frame.

[9] Implemented in `Python` using the `scikit-learn` package (`https://scikit-learn.org/`).

and 3/4 of the time arc of the cluster and we measured the maximum distance between estimated positions of the tracklets in the cluster (namely, the *cluster error*). Finally we left the repeated tracklet in the cluster that had the smallest *cluster error* and we removed it from the other clusters it belonged to.

REFERENCES

Armitage, P. J. 2017, arXiv:astro-ph/0701485v6

Astropy Collaboration, Price-Whelan, A. M., Sipőcz, B. M., et al. 2018, AJ, 156, 123

Astropy Collaboration, Robitaille, T. P., Tollerud, E. J., et al. 2013, A&A, 558, 33

August, T. M., & Wiegert, P. A. 2013 AJ, 145, 152

Bernstein, G., & Khushalani, B. 2000, AJ, 120, 3323

Bernstein, G. M., Trilling, D. E., Allen, R. L., Brown, M. E., Holman, M., & Malhotra, R. 2004, AJ, 128, 1364

Bhattacharya, B., Noriega-Crespo, A., Penprase, B. E., et al. 2010, ApJ, 720, 114

Bowell, E., Hapke, B., Domingue, D., et al. 1989, in Asteroids II, ed. R. P. Binzel, T. Gehrels, & M. Shapley Matthews (Tucson, AZ: Univ. Arizona Press), 524

Cabrera-Vives, G., Reyes, I., Förster, F., Estévez, P. A. & Maureira, J. C. 2017, ApJ, 836, 97

Carey, S. J., Noriega-Crespo, A., Mizuno, D. R., et al. 2009, PASP, 121, 76C

Dandy, C. L., Fitzsimmons, A. & Collander-Brown, S. J. 2002, Icarus, 163, 363D

DeMeo, F. E., & Carry, B. 2013 Icarus, 226, 723

DeMeo, F. E., & Carry, B. 2014 Nature, 505, 629

DePoy, D. L., Abbott, T., Annis, J., et al. 2008, Proc. SPIE, 7014, 70140E

Dohnanyi 1969 , J. Geophys. Res., 74, 2531

Foreman-Mackey, D., Hogg, D. W., Lang, D. & Goodman, J. 2013, PASP, 125, 306

Förster, F., Maureira, J. C., San Martín, J., et al. 2016, ApJ, 832, 155

Förster, F., Moriya, T. J., Maureira, J. C., et al. 2018, Nature Astronomy, 2, 808F

Fuentes, C. I., George, M. R. & Holman, M. J. 2009, ApJ, 696, 91

Fuentes, C. I., & Holman, M. J. 2008, AJ, 136, 83

Fukugita, M., Ichikawa, T., Gunn, J. E., et al. 1996, AJ, 111, 1748F

Gladman, B., Davis, D. R., Neese, C., et al. 2009, Icarus, 202 (2009) 104-118

Gladman, B., Marsden, B. G., & Vanlaerhoven, C. 2008, in The Solar System Beyond Neptune (Tucson, AZ: Univ. Arizona Press), 43

Goodman, J. & Weare, J. 2010, CAMCS, 5, 65

Holman, M. J., Payne, M. J., Blankley, P., et al. 2018 AJ, 156 135

Horner, J., Koch, F. E. & Lykawka, P. S 2013, arXiv:1302.2304

Ivezić, Ž., Jurić, M., Lupton, R. H., et al. 2010, NASA Planetary Data System, 124

Ivezić, Ž., Kahn, S. M., Tyson, J. A., et al. 2018, ApJ, 873, 111

Ivezić, Ž., Tabachnik, S., Rafikov, R., et al. 2001, AJ, 122, 2749

Jewitt, D. 2015, AJ, 150, 201J

Krisciunas, K., Margon, B. & Szkody, P. 1998, PASP, 110, 1342K

Lamy, P. & Toth, I 2009, Icarus, 201, 674L

Lin, H. W., Yoshida, F., Chen, Y. T., et al. 2015 Icarus, 254, 202L

LSST Science Collaborations, Abell, P. A., Allison, J., et al. 2009, arXiv:0912.0201

Lykawka, P. S. & Mukai, T. 2007, Icarus, 189, 213L

Martínez-Palomera, J., Förster, F., Protopapas, P., et al. 2018, AJ, 156, 186M

Masiero, J. R., Mainzer, A. K., Grav, T., et al. 2011 ApJ, 741, 68

Medina, G. E., Muoz, R. R., Vivas, A. K., et al. 2017, ApJ, 845L, 10M

Medina, G. E., Muoz, R. R., Vivas, A. K., et al. 2018, ApJ, 855, 43M

Parker, A., Ivezić, Ž., Jurić, M., Lupton, R., Sekora, M. D. & Kowalski, A. 2008, Icarus, 198, 138

Peña, J., Fuentes, C., Förster, F., et al. 2018, AJ, 155 135

Pike, R. E., Fraser, W. C., Schwamb, M. E., et al. 2017, AJ, 154, 101P

Polishook, D., Ofek, E. O., Waszczak, A., et al. 2012, MNRAS, 421, 2094P

Rebull, L. M., Padgett, D. L., McCabe, C. -E., et al. 2010, ApJS, 186, 259R

Ryan, E. L., Mizuno, D. R., Shenoy, S. S., et al. 2015, A&A, 578, 42.

Ryan, E. L., Woodward, C. E., Dipaolo, A., et al. 2009, AJ, 137, 5131R

Schechter, P., & Press, W. H. 1976, ApJ, 203, 557

Schlafly, E. F., Green, G. M., Lang, D., et al. 2018 ApJS, 234, 39S

Sheppard, S. S. & Trujillo, C. A. 2006, Science, 313, 511

Sheppard, S. S. 2010, AJ, 139, 1394S

Solontoi, M., Ivezić, Ž; Jurić, M., et al. 2012, Icarus, 218, 571S

Terai, T., Yoshida, F., Ohtsuki, K., et al. 2018, PASJ, 70S, 40T

Vaduvescu, O., Aznar Macias, A., Tudor, V., et al. 2017, EM&P, 120, 41V

Waszczak, A., Chang, C.-K., Ofek, E. O., et al. 2015, AJ150, 75

Wiegert, P., Balam, D., Moss, A., et al. 2007 AJ, 133, 1609

Wright, E. L., Eisenhardt, P. R. M., Mainzer, A. K. et al. 2010 AJ, 140, 1868

York, D. G., Adelman, J., Anderson, J. E., et al. 2000, AJ, 120, 1579

Yoshida, F., Nakamura, T., Watanabe, J. I., et al. 2003 PASJ, 55, 701

Yoshida, F. & Nakamura, T. 2007 Planet. Space Sci., 55, 1113Y